## STRUCTURAL BIOLOGY

# Cryo-EM and MD infer water-mediated proton transport and autoinhibition mechanisms of $V_o$ complex

Soung-Hun Roh[1]*†, Mrinal Shekhar[2,3]*, Grigore Pintilie[4], Christophe Chipot[3,5], Stephan Wilkens[6†], Abhishek Singharoy[2†], Wah Chiu[4,7†]

Rotary vacuolar adenosine triphosphatases (V-ATPases) drive transmembrane proton transport through a $V_o$ proton channel subcomplex. Despite recent high-resolution structures of several rotary ATPases, the dynamic mechanism of proton pumping remains elusive. Here, we determined a 2.7-Å cryo–electron microscopy (cryo-EM) structure of yeast $V_o$ proton channel in nanodisc that reveals the location of ordered water molecules along the proton path, details of specific protein-lipid interactions, and the architecture of the membrane scaffold protein. Moreover, we uncover a state of $V_o$ that shows the $c$-ring rotated by ~14°. Molecular dynamics simulations demonstrate that the two rotary states are in thermal equilibrium and depict how the protonation state of essential glutamic acid residues couples water-mediated proton transfer with $c$-ring rotation. Our cryo-EM models and simulations also rationalize a mechanism for inhibition of passive proton transport as observed for free $V_o$ that is generated as a result of V-ATPase regulation by reversible disassembly in vivo.

## INTRODUCTION

Active proton transport is central to controlling the balance between cellular pH and efficiency of energy metabolism. Vacuolar adenosine triphosphatases (V-ATPases) are adenosine 5′-triphosphate (ATP) hydrolysis–driven rotary motor proton pumps that acidify the lumen of subcellular organelles in virtually every eukaryotic cell (*1–3*). V-ATPase is organized in cytosolic $V_1$-ATPase and membrane-bound $V_o$ proton channel subcomplexes that are coupled by a rotating central stalk and three peripheral stators (fig. S1A) (*4*). $V_o$ proton channel operates by a conserved mechanism that involves clockwise rotation (as seen from the cytosol) of a ring of 10 "proteolipid" or $c$ subunits (proteolipid- or $c$-ring; $c_8c'c''$ in yeast) past the C-terminal transmembrane domain of subunit $a$ ($a_{CT}$). Each proteolipid subunit has one lipid-exposed glutamic acid residue that carries protons from a cytosolic to a luminal aqueous half-channel located within $a_{CT}$. Direct proton flow between the two half-channels is blocked by two arginine residues in the middle of the bilayer that transiently engage the $c$ subunits' glutamates in a salt bridge during $c$-ring rotation. Eukaryotic V-ATPase is regulated by a mechanism referred to as "reversible disassembly," wherein $V_1$-ATPase detaches from membrane-bound $V_o$ in a nutrient-dependent manner (*5*). Upon disassembly of the holoenzyme, both $V_o$ and $V_1$ subcomplexes become autoinhibited, with the membrane-detached $V_1$ losing the ability to hydrolyze MgATP and the free $V_o$ becoming impermeable to protons (fig. S1B) (*6*).

Cryo–electron microscopy (EM) (cryo-EM) has been used to characterize structural details of several rotary ATPases including F- and A/V-type ATP synthases (*7–10*). However, the dynamic mechanism

of proton pumping and the role of water in the process remain elusive. Here, we integrate a 2.7-Å cryo-EM structure of yeast $V_o$ in lipid nanodisc ($V_o$ND) with extensive molecular dynamics (MD) simulations. We identify the locations of ordered water molecules and the presence of another structural state, which differs by a ~14° rotation of the $c$-ring, findings that agree well between experiments and simulations. Moreover, the simulations show that proton transfer from the $c$-ring glutamates to the luminal half-channel in $a_{CT}$ involves transient water wires, reminiscent of the classic alternating-access mechanism of membrane transport (*11*). Together, our studies rationalize the energetics of $c$-ring rotation-driven proton transport and the molecular basis for $V_o$ autoinhibition.

## RESULTS

### Cryo-EM structure of $V_o$ND at 2.7-Å resolution

Using a dataset of >700,000 $V_o$ND particle images, we were able to reconstruct a 3.1-Å map of the complex. Furthermore, three-dimensional (3D) classification resulted in five distinct reconstructions solved at resolutions between 2.7 and 3.6 Å (fig. S2). The 2.7-Å map of $V_o$ND (Fig. 1A and movie S1) resembles a conformation of the complex as seen in previous lower-resolution structures (*12–14*) but reveals finer structural details for residues involved in proton transport, including those of $a_{CT}$'s transmembrane helices 7 and 8 (Fig. 1A, bottom) and the $c$-ring (Fig. 1B). The cryo-EM densities for glutamic acid residues exposed to the lipid bilayer indicate a "proton-locked" conformation [as seen in crystal structures of $c$-rings of related rotary ATPases (*15*)]. For instance, the carboxyl groups of $c_{(2)}$E137 and $c'$E145 are in hydrogen bonding distance to the backbone carbonyl oxygens of $c_{(2)}$M59 and $c'$M67, respectively (Fig. 1B, bottom left and right insets). In contrast, there is little EM density beyond $c_{(1)}$E137's γ carbon (Fig. 1B, top left inset), suggesting that its carboxyl group is deprotonated. $c''$E108, on the other hand, appears well resolved (Fig. 1B, top right inset), consistent with its carboxyl group forming a salt bridge with $a_{CT}$'s R735.

The 2.7-Å map also resolved several ordered lipid molecules, some of which form a bilayer within the central cavity of the $c$-ring, presumably to prevent transmembrane leakage of protons and other ions (Fig. 1C and fig. S3A). Several individual lipid molecules seen

[1]School of Biological Sciences, Seoul National University, Seoul 08826, South Korea. [2]Biodesign Institute, School of Molecular Sciences, Arizona State University, Tempe, AZ 85801, USA. [3]Department of Physics, University of Illinois at Urbana-Champaign, Urbana, IL 61801, USA. [4]Department of Bioengineering, James H. Clark Center, Stanford University, Stanford, CA 94305, USA. [5]Laboratoire International Associé CNRS-UIUC, UMR 7019, Université de Lorraine, 54506 Vandœuvre-lès-Nancy, France. [6]Department of Biochemistry and Molecular Biology, SUNY Upstate Medical University, Syracuse, NY 13210, USA. [7]Division of Cryo-EM and Bioimaging, SSRL, SLAC National Accelerator Laboratory, Stanford University, Menlo Park, CA 94025, USA.
*These authors contributed equally to this work.
†Corresponding author. Email: wahc@stanford.edu (W.C.); shroh@snu.ac.kr (S.-H.R.); asinghar@asu.edu (A.S.); wilkenss@upstate.edu (S.W.)
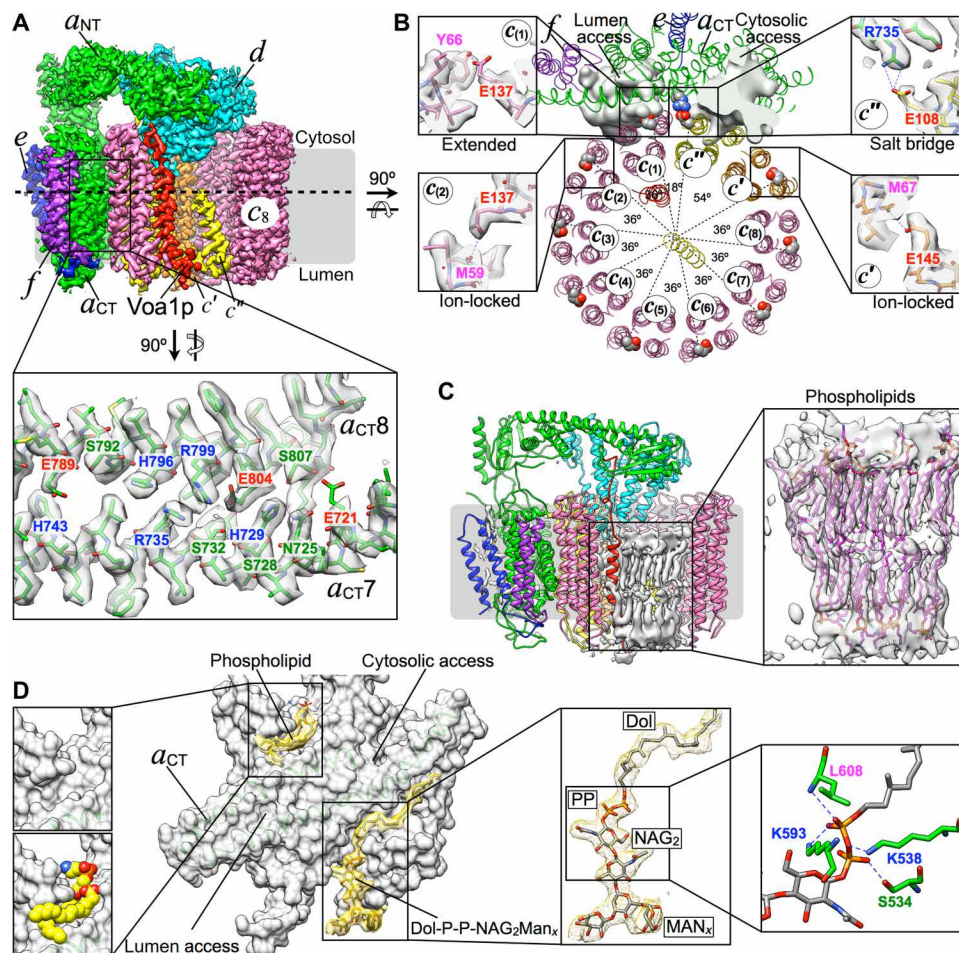
**Fig. 1. A 2.7-Å cryo-EM structure of yeast $V_o$ in lipid nanodisc.** (**A**) A 2.7-Å map of $V_o$ND showing subunits $a$ (green), $d$ (cyan), $c_8$ (pink), $c'$ (orange), $c''$ (yellow), $e$ (blue), $f$ (purple), and Voa1p (red). The densities for two of the $c$ subunits are removed to allow a view inside the $c$-ring. Inset, $a_{CT}$ TM α helices 7 and 8 fitted to the cryo-EM density. The annotations of the amino acids follow the traditional color codes of their types. (**B**) Cross section of the $V_o$ model as indicated by the dashed line in (A). The cytosolic and luminal half-channels are indicated by gray density. The essential glutamic acids of the $c$-ring are highlighted in spacefill representation. The densities for E137 of $c_{(1)}$ and $c_{(2)}$, E108 of $c''$, and E145 of $c'$ are shown in the insets. Distances consistent with hydrogen bond formation to nearby residues are indicated by dashed lines. (**C**) The central cavity of the $c$-ring is occupied by lipid molecules (modeled as phosphatidylethanolamine) that are forming a bilayer. (**D**) Surface representation of $a_{CT}$ as seen from the $c$-ring showing two cavities (next to the cytosolic and luminal half-channels) that are occupied by nonproteinaceous densities. The cavity on the cytosolic side is occupied by a tightly bound phospholipid (left). The cavity open to the luminal side is occupied by density that we modeled as the glycosylation precursor dolichol-P-P-(GlcNAc)$_2$Man$_x$ (right). The pyrophosphate moiety is stabilized by the side chains of $a$K538, $a$K593, $a$S534, and the backbone amide of $a$L608.

at the periphery of $a_{CT}$ and subunits $e$ and $f$ likely contribute to the stability of the complex (fig. S3B). Next to the cytosolic and luminal half-channels that provide water access to the $c$-ring glutamates (Fig. 1B, gray density), $a_{CT}$ has two additional cavities, one open to the cytosol and another toward the lumen (Fig. 1D, middle). The cavity that opens to the cytosol is occupied by a tightly bound lipid molecule that prevents direct access for water molecules from the cytoplasm to the $c$-ring (Fig. 1D, left). A cavity that opens to the lumen side of $a_{CT}$ is occupied by a nonproteinaceous density, which was already resolved in previous lower-resolution maps of $V_o$ prepared by different biochemical protocols (12–14). On the lumen side of the complex, the density for this molecule resembles a branched carbohydrate linked via a pyrophosphate (PP) moiety to an aliphatic hydrocarbon tail, which can be traced to the middle of the membrane (Fig. 1D, middle). We modeled this density as mannosyl$_x$-$N$-acetylglucosaminyl$_2$-diphospho dolichol (Fig. 1D, right), the

common precursor for the oligosaccharyltransferase machinery that is synthesized on the cytosolic side of the endoplasmic reticulum (ER) and then flipped into the ER lumen. Our assignment of pyrophosphate is supported by the fit of the model to the density (fig. S3C, right), and the charge complementarity of the phosphates with lysines $a$K538 and $a$K593 (Fig. 1D, right). Both lysines are strictly conserved and known to play a critical role in the assembly of the complex in yeast (16), suggesting that this dolichol-linked carbohydrate may have an essential role in the stability of subunit $a$ during $V_o$ assembly.

## Membrane scaffold proteins stabilize $V_o$

Our cryo-EM maps of $V_o$ND displayed several belt-like densities wrapping around the membrane-exposed parts of the $c$-ring and $a_{CT}$. Similar features have been described for other nanodisc-embedded membrane proteins and were ascribed to the Apolipoprotein (Apo) A1–derived membrane scaffold protein (MSP) used for nanodisc

reconstitution (*17*). Unexpectedly, focused classification revealed three distinct tubular densities wrapped around the bilayer exposed region of the *c*-ring (Fig. 2A), with the density at the periphery of $a_{CT}$ less well resolved (fig. S4). Two of the tubular densities are near the cytosolic side, with a third one close to the luminal side of the complex (Fig. 2B). The distance between the two belts at the cytosolic side of ~13 Å is essentially identical to the distance between two protomers of Apo A1 as seen in its crystal (1av1) and nuclear magnetic resonance (6cc9) structures (*18*, *19*). The presence of a third belt suggests that a canonical MSP dimer is not sufficient to stabilize the hydrophobic surface of the *c*-ring, which is substantially wider (~40 Å) compared to the membrane spanning α helices of, for example, transient receptor potential vanilloid 5 (TRPV5) (30 Å; 6o1u) (*20*). While the top and bottom belts appear to be in direct contact with residues of the *c*-ring (Fig. 2B, left and right, and fig. S4), the middle belt leaves sufficient space (~15 Å) to accommodate bulk lipid (Fig. 2B, middle). Together, this arrangement of the MSPs, as seen in our cryo-EM map of $V_oND$, provides a rationale for the improved stability of the nanodisc-reconstituted complex.

## Protonation states of essential glutamates control water channel access

In our 2.7-Å map, we placed water molecules into density peaks using the "Find Waters" routine available in Coot (see Materials and Methods) (Fig. 3, A and B). To evaluate the authenticity of the putative water molecules, we computed the *Q*-score, which measures the resolvability of the atoms (Fig. 3B, left) (*21*), and the distance between water and the adjacent oxygen and nitrogen atoms (fig. S5A). Both these measurements are within the range of expected values for either crystal or cryo-EM structures (*21*, *22*). Further support for the authenticity of the modeled water in our 2.7-Å map comes from the presence of densities resembling water molecules between Q80's side chain and V7's carbonyl oxygen in all eight copies of the *c* subunits [$c_{(1)-(8)}$] (fig. S5B). Using this protocol, we modeled a total of ~180 water molecules, ~40 of which are within the putative proton path (Fig. 3, A and B, and fig. S5C). Most notable are water molecules connecting the side-chain nitrogens of $a$R799 to the cytosolic entry channel and between $c_{(1)}$E137's carboxyl group and the side chain of $a$H796 (Fig. 3B, see arrowheads in left panel).

To further validate the water assignments, we carried out all-atom MD simulations starting with the model derived from our 2.7-Å map embedded in bulk water (i.e., water standard density in randomized positions). Compared to protein motion, which takes up
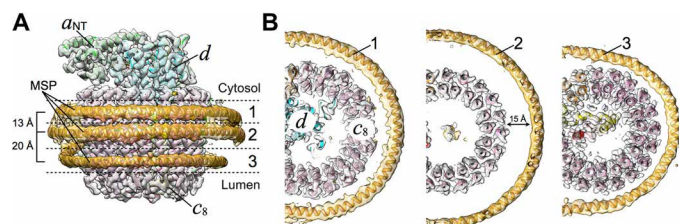
to milliseconds, water molecules move on the nanosecond time scale. By overlaying a large number of individual MD coordinate frames, a residence probability map of stably bound water molecules can be obtained (Fig. 3C, blue dots). The positional overlap of the statistically probable water clusters in the simulations and the putative water molecules detected in the cryo-EM density is notable (compare red beads and blue dots in Fig. 3C, and see fig. S6). This overlap not only supports the validity of the cryo-EM map–derived water assignment but also demonstrates the usefulness of near-atomic resolution cryo-EM structure–based MD simulations in the context of biochemical activity. The fact that some MD-derived water clusters are not clearly resolved in the cryo-EM map (and vice versa) could be due to (i) the extent of positional accuracy in the 2.7-Å cryo-EM structure, (ii) the assumptions imposed by the classical force field used in the MD simulations, and (iii) the difference in the temporal scales of the cryo-specimen plunge freeze and the simulations. Whereas the cryo-EM density represents an average of multiple chemical states present during the millisecond time frame of plunge freezing, classical MD can capture only one state at a time on a nano- to submillisecond time scale (*23*). Nevertheless, the simulations identify charged and polar residues in the luminal and cytosolic half-channels that form hydrogen bonds to the ordered water, keeping the water columns stable in both channels (fig. S7).

Next, we performed two separate MD simulations to explore the role of water dynamics in the transfer of the proton from essential *c*-ring glutamates to the luminal half-channel in $a_{CT}$ (fig. S8, A and B). In eukaryotic V-ATPase, a critical residue involved in this process is a strictly conserved glutamic acid ($a$E789 in yeast) that is located at the entry of the luminal half-channel across from $c_{(1)}$E137 (Fig. 3B). In the first simulation, the donating $c_{(1)}$E137 was protonated, and the receiving $a$E789 was deprotonated (Fig. 3D, left). In the second simulation, the protonation states of the two residues were reversed (Fig. 3D, right). The simulated dynamics of the water molecules suggests that proton transfer from *c*-ring glutamic acid residues ($c$E137, $c'$E145, or $c''$E108) to $a$E789 occurs via a cluster of water molecules, whose lifetime depends on the protonation states of the two residues. At the onset of the transfer, when a proton resides on, e.g., $c_{(1)}$E137, a network of hydrogen-bonded water molecules (hereafter referred to as "water wire") connects the carboxyl groups of $c_{(1)}$E137 and $a$E789 for >50% of the structures derived from three independent 500-ns simulations (Fig. 3E, blue vertical lines). These water wires enable transfer of the proton from *c*-ring essential glutamates to $a$E789 (Fig. 3F). After the transfer, when the *c*-ring glutamate is ionized, and $a$E789 is protonated, no water wires are observed in the simulation (Fig. 3E, red line). This disruption of the water wire after proton transfer ensures that protons cannot leak back from the luminal half-channel into the $a_{CT}$:*c*-ring interface once proton transfer has occurred. Note that some water molecules are retained near $c_{(1)}$E137 after deprotonation (Fig. 3G), likely to stabilize the newly ionized glutamic acid. The negatively charged $c_{(1)}$E137 is also stabilized by transient hydrogen bond formation with $c_{(1)}$Y66 as observed in the 2.7-Å map (Fig. 1B, top left inset, and fig. S9). Together, dynamics of the water wires is coupled to the charge and conformational states of key acidic residues for controlling proton transport during *c*-ring rotation.

## Another rotary state of autoinhibited $V_o$

Aside from the 2.7-Å map, which is representative of the dominant population of autoinhibited $V_oND$ (~95%; Fig. 4A), 3D classification
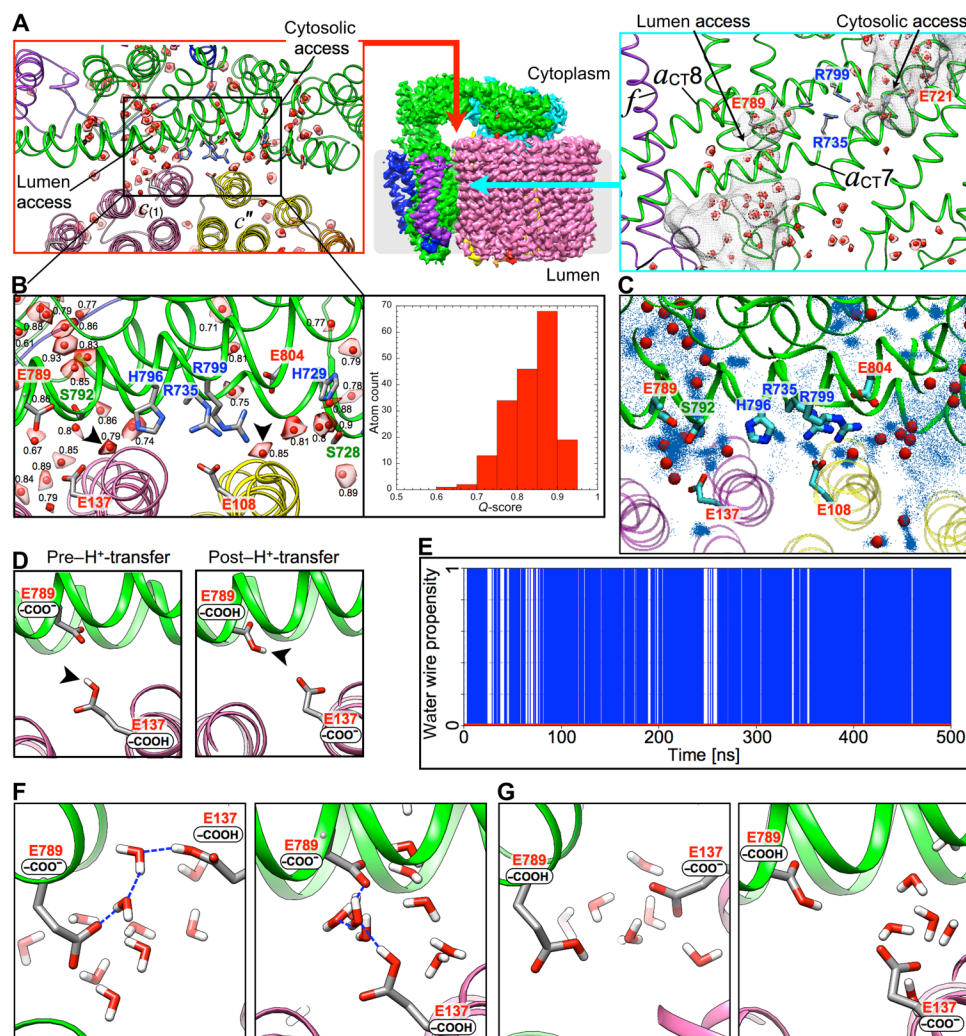


**Fig. 2. MSPs stabilize nanodisc reconstituted $V_o$ proton channel.** (**A**) Focused classification resolves three distinct belts of density that surround the membrane-exposed surface of the *c*-ring. The three belts were modeled as one canonical dimer and one monomer of MSP. (**B**) The three belts show varying distances to the *c*-ring. Whereas the middle belt leaves sufficient space to accommodate a layer of lipid molecules, the upper and lower belts appear to directly contact and stabilize the *c*-ring, presumably via hydrophobic residues of MSP that are oriented toward the *c* subunits.

**Fig. 3. Water molecules at the $a_{CT}$:$c$-ring interface.** (**A**) Cryo-EM density at the $a_{CT}$:$c$-ring interface that is modeled as ordered water molecules. Water molecules are represented as red spheres with surrounding density contoured at 0.025 (2.5 root mean square deviation). (**B**) Left: Zoomed-in view of the interface with modeled water molecules and their $Q$-scores. Right: Histogram of $Q$-scores for modeled water molecules. (**C**) Overlap of the experimentally assigned water molecules (red beads) with computationally derived water occupancy across a 0.5-μs MD simulation (blue dots). (**D**) Water dynamics was simulated in the pre–H$^+$-transfer state [$c_{(1)}$E137 protonated, $a$E789 deprotonated; left image] and post–H$^+$-transfer state [$c_{(1)}$E137 deprotonated, $a$E789 protonated; right image]. (**E**) Occurrence of water wires with 5000 frames accumulated over 0.5-μs MD simulations indicated by blue vertical lines for the pre–H$^+$-transfer state. No water wires were observed for the post–H$^+$-transfer state as indicated by the red line. (**F**) Two views of a representative coordinate frame with water-wire connecting $c_{(1)}$E137 and $a$E789 in the pre–H$^+$-transfer state. The left image is seen parallel to the membrane toward the $a_{CT}$:$c$-ring interface. The right image is seen perpendicular to the membrane along the $a_{CT}$:$c$-ring interface. Hydrogen and oxygen atoms are shown in white and red, respectively. (**G**) Representative coordinate frame with $c_{(1)}$E137 and $a$E789 seen in the post–H$^+$-transfer state. The two different views are as in (F). The protonated $a$E789 blocks access for water molecules from the luminal channel. A few water molecules are retained near the ionized $c_{(1)}$E137.

revealed a minor, hitherto unseen autoinhibited rotary state solved at 3.6 Å (~5%, class 4) (Fig. 4B). This minor substate population showed the $c$-ring/subunit $d$ subcomplex rotated by ~14° relative to $a_{CT}$ in the direction of proton pumping. This clockwise rotation of the $c$-ring brings $c_{(1)}$E137 close to $a_{CT}$'s two arginine residues R735/799 and exposes $c''$E108 to bulk water entering from the cytosolic half-channel (see arrow in Fig. 4B). The 14° rotation of the $c$-ring/$d$ subcomplex did not lead to disruption of the binding interface between the distal end of $a_{NT}$ and subunit $d$, resulting in a compression/outward bending of $a_{NT}$'s coiled-coil segment (Fig. 4, C and D; fig. S10; and movie S2). Therefore, autoinhibited V$_o$ in lipid nanodisc can exist in at least two distinct states: the previously described, predominant

state 3 (*12–14*), and a less abundant state, hereafter referred to as state 3′.

## Free energy landscape of $c$-ring rotation suggests molecular origins of autoinhibition

Unlike the isolated membrane sector of F-ATP synthase, F$_o$, which acts as a passive proton pore (*24*), free V$_o$ does not conduct protons along a pH gradient under physiological conditions (*25*). The molecular origin of this difference in activity between the two related proton channel subcomplexes is not known. To explore the energetics of side-chain interactions in the autoinhibited state and during $c$-ring rotation, we applied MD simulations to the 2.7-Å state 3 model
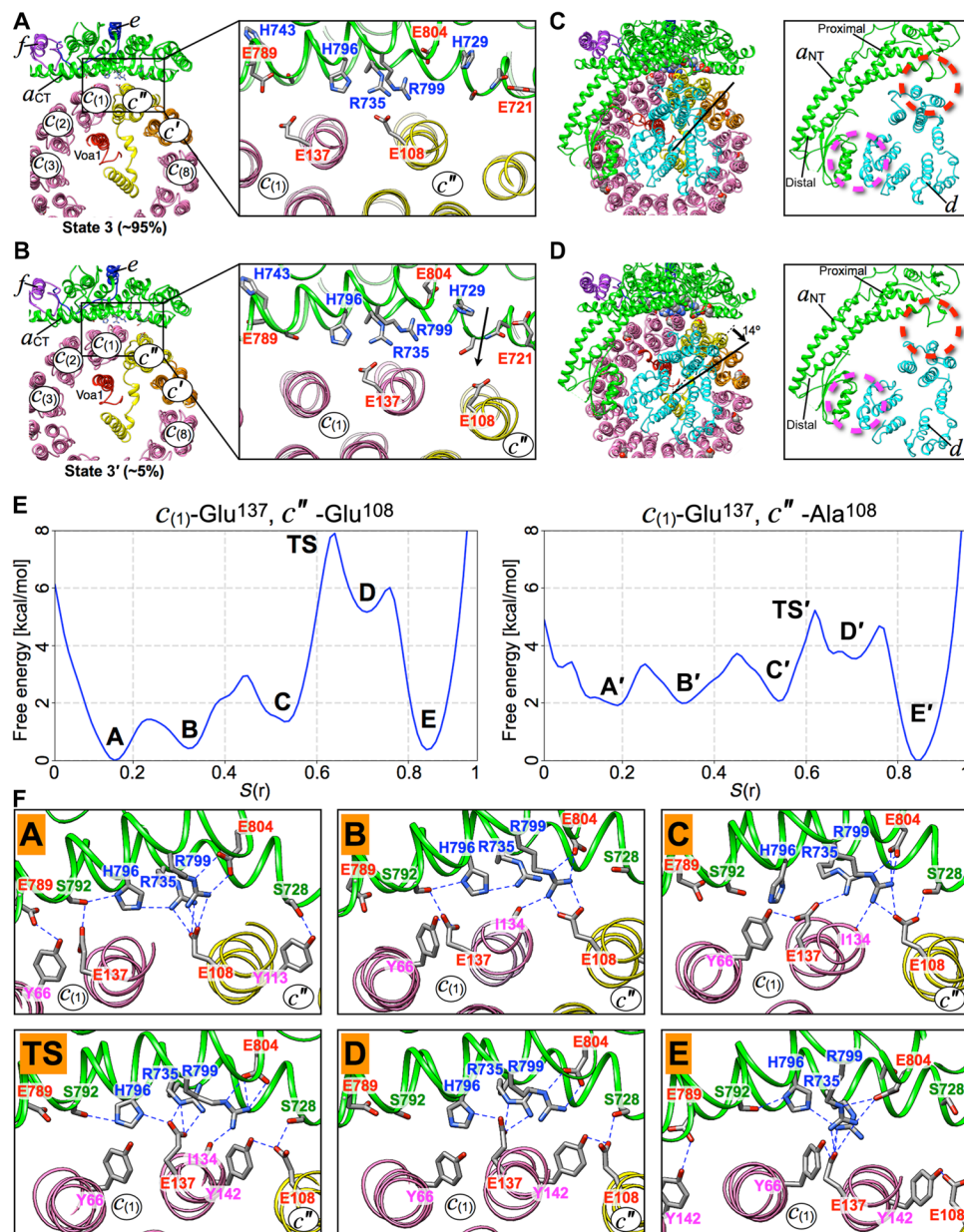
**Fig. 4. Two rotary states of autoinhibited yeast $V_o$.** About 95% of all particles in the final cryo-EM dataset of $V_o$ND, including the particles that constitute the 2.7-Å structure (**A**), represent rotary state 3. (**B**) 3D classification of the final dataset revealed a minor population of particles (~5%) that represent a state different from the hitherto described autoinhibited state (state 3) of the complex. In this minor state, which is designated state 3′, the $c$-ring is rotated clockwise in the direction of proton pumping by about 14°. This rotation of the $c$-ring brings E137 of $c_{(1)}$ close to $a_{CT}$'s two essential arginine residues. (**C** and **D**) Whereas the $d$:$a_{NT}$ interaction at the distal domain of $a_{NT}$ seen in the predominant state 3 is preserved in the minor state 3′ (pink dashed circles), the interaction at $a_{NT}$'s proximal domain is not (red dashed circles). (**E**) Free energy profile of $c$-ring rotation for wild type ($c''$E108; left) and mutant ($c''$E108A; right). $c$-ring rotation was simulated using a biasing potential within a solvated membrane to induce a clockwise motion of the ring. (**F**) Wild-type coordinate files were extracted from the simulation near the energy minima designated as substates A to E in the left panel of (E). Substate TS represents the high-energy transition between substates C and D. Some of the polar residues in the $a_{CT}$:$c$-ring interface are highlighted by stick representation. Distances consistent with hydrogen bond formation are indicated by the blue dashed lines.

of the $V_o$. However, even in fully active holo V-ATPase, ATP hydrolysis–driven clockwise rotation of one $c$-ring glutamic acid past $a_{CT}$ occurs on the millisecond time scale [~18 μmol/(min × mg) => ~300 ATP/s => ~100 rps => ~1000 H⁺/s => ~1 H⁺/ms (26)], with a substantially slower dynamics expected for autoinhibited $V_o$. This time scale remains, however, beyond the reach of standard, all-atom MD simulations for membrane protein complexes the size of $V_o$. To capture such millisecond—or even slower rotation events, we combined string optimization with adaptive biasing force simulations (see Materials and Methods for details) (27–29). Our calculations reveal the most favorable reaction path on the free energy landscape of $c$-ring rotation, showing five distinct minima referred to as substates A, B,

C, D, and E (Fig 4E, left, and movies S3 and S4). Substate A has the lowest free energy as it results from the initial MD equilibration of the 2.7-Å state 3 model (compare Fig. 4, A and F, top left). Subsequent rotation of the $c$-ring follows an uphill free energy path via three local minima, B, C, and D, before reaching substate E, which has a free energy similar to substate A. While all substates show interaction of the two $c$-ring glutamates and $a_{CT}$'s two arginines (Fig 4F), the higher free energy (lower stability) of substates B, C, and D suggests that some of the inter- and intra-subunit interactions at the $a_{CT}$:$c$-ring interface are lost, or strained, in these intermediates. Such a destabilizing effect is most prominent in the transition between substates C and D via the "transition state" (TS), which involves the disruption of the interaction of $c''$E108 with the two arginines (Fig 4F, bottom left). The transition between C and D is the rate-limiting step of the ~14° $c$-ring rotation connecting substates A and E and requires an activation energy of ~6.5 kcal/mol, corresponding to a time constant of ~110 ms (see Materials and Methods for kinetics calculations). Together, the free energy profile underlying the rotation pathway reveals that the $a_{CT}$:$c$-ring interface is dominated by the electrostatic attraction between the $c$-ring essential glutamates [$c_{(1)}$E137 and $c''$E108] and the $a_{CT}$ essential arginines ($a$R735 and $a$R799) and that disruption of one of these interactions represents the slowest step of the 14° rotation from A to E. It is noteworthy that the simulated substate E resembles the experimentally determined cryo-EM structure of state 3′ (compare Fig. 4, B and F, bottom right), a finding that lends supports to our simulation protocol.

The simulation described above started from the autoinhibited state, which is a unique rotary state due to the presence of two carboxylic acids in the $a_{CT}$:$c$-ring interface [$c_{(1)}$E137 and $c''$E108; Fig. 4A]. During regular function of this motor, however, only a single glutamate is at the interface for most of the time, with the two neighboring carboxyls of $c_{(1)}$ and $c''$ moving past $a_{CT}$ only once every 360° rotation of the $c$-ring. We, therefore, performed a second simulation with the same starting model, albeit wherein $c''$E108 was mutated to alanine ($c''$E108A), so that only a single carboxylic acid [$c_{(1)}$E137] is at the interface. The $c''$E108A mutant abolishes the interaction of this residue with the $a_{CT}$ essential arginines ($a$R735 and $a$R799), thus mimicking $c$-ring rotation when a single E137 from subunits $c_{(2)}$-$c_{(8)}$ (or E145 from $c'$) moves past $a_{CT}$, as it occurs during active proton pumping by the holo V-ATPase. The MD simulation of this mutant complex generated substates A′ to E′ (Fig. 4E, right). Noteworthily, while the number of free energy minima is unchanged, the $c''$E108A mutation reduces the free energy barrier, TS′, by ~40% compared to the wild type (Fig. 4E, left). The lower free energy barrier of TS′ makes the clockwise rotation from A′ to E′ thermally accessible within ~0.6 ms, in contrast with the ~110 ms for the rotation from A to E with the unique autoinhibited state, whereby both $c_{(1)}$E137 and $c''$E108 are at the interface. In addition, the time constant for the counterclockwise uphill movement in the E′-to-A′ direction was estimated to be ~20 ms.

The simulated rotations between A and E, and A′ and E′, cover two of the possible transitions that occur during a complete 360° rotation of the $c$-ring in an isolated $V_o$: a unique transition with two glutamates at the interface (the "2-glu" transition between A and E) and the transition where only one glutamate moves past $a_{CT}$ (the "1-glu" transition between A′ and E′, which occurs eight times) (fig. S11A). However, because of the asymmetry of the $c$-ring (Fig. 1B), there is a third possible transition with no glutamic acid at the interface (the "0-glu" transition between $c''$E108 and $c'$E145). Because the

total path of the $0$-glu transition is ~3 times longer than that of the simulated A′-to-E′ transition (36 Å versus 12 Å, respectively), and despite the similar end-point free energies, an even larger time constant of ~180 ms can be extrapolated for this transition (see legend to fig. S11 for calculation). Thus, we consider a number of distinct transitions that characterize the overall $c$-ring rotary dynamics in an isolated $V_o$ (fig. S11A) and find that the $0$-glu transition represents the slowest step, followed by the $2$-glu and $1$-glu transitions.

## DISCUSSION

The biological implications of these simulation results are as follows: During ATP hydrolysis–driven proton pumping in holo V-ATPase, the $c$-ring rotates clockwise to carry protons from the cytosolic to the luminal half-channel. Upon regulated detachment of $V_1$-ATPase from $V_o$, any existing proton gradient is expected to push the $c$-ring in the opposite (counterclockwise) direction to allow for the reverse flow of protons. As mentioned above, an isolated $V_o$ from the eukaryotic V-ATPase has evolved to efficiently block such passive proton leakage (25) in contrast with $F_o$, which allows some passive transport (24). In the autoinhibited state of the $V_o$ complex, which is represented by states 3 and 3′, both glutamic acids, $c_{(1)}$E137 and $c''$E108, are at the $a_{CT}$:$c$-ring interface (Fig. 4, A and B). Whereas the $a_{NT}$:$d$ and $d$:$c$-ring interactions can accommodate the ~14° $c$-ring rotation between these two states (Fig. 4, C and D; fig. S10; and movie S2), it is obvious that clockwise or anticlockwise rotation beyond either state would require the disruption of at least one of these interactions. Because the interaction of $a_{NT}$ and $d$, which is only seen in free $V_o$, links the stator (subunit $a$) to the rotor ($c$-ring-$d$ subcomplex) of the $V_o$ motor, it has been proposed that this interaction is responsible for autoinhibition (30). However, we and others have previously reported that removal of either $a_{NT}$ or $d$ from $V_o$ does not result in measurable proton transport (31, 32). This suggests that $V_o$ autoinhibition must be ascribed to additional thermodynamic or kinetic factors that distinguish between the $V_o$ and $F_o$ proton channels.

The most notable difference between the two systems lies in the structure of the $c$-ring, featuring identical transitions in $F_o$, in contrast with the three distinct transitions in $V_o$ arising from the unique structure of $c''$ (Fig. 1B and fig. S11). From the three $c$-ring transitions in $V_o$, the $2$-glu transition is both structurally and kinetically similar to the $c$-ring rotation in free $F_o$ because it features neighboring glutamic acids at the interface and occurs at a rate similar to that of passive proton transport in $F_o$ (fig. S11B) (24). This means that while the "$F_o$-like" $2$-glu transition in $V_o$ contributes substantially to autoinhibition, it is unlikely to be the sole cause, as the corresponding transitions in $F_o$ allow for some passive transport (~3% of $F_1F_o$ activity) (24, 33). The $1$-glu transition occurs within ~0.6 or ~20 ms, depending on the direction of $c$-ring rotation, which is notably faster than the $2$-glu transition. This suggests that the unique $0$-glu transition, estimated to take at least ~180 ms, represents a rate-limiting component of $c$-ring rotation. The dominant role of the $0$-glu transition is also supported by mutagenesis experiments. Mutating either $c''$E108 or $c'$E145 results in complete inhibition of proton pumping by the holoenzyme (34), indicating that when the length of the $0$-glu transition is increased to a three or four helix gap, even the free energy of ATP hydrolysis is insufficient to drive $c$-ring rotation.

In summary, our cryo-EM structures of states 3 and 3′, together with the MD-derived free energy profiles and kinetic constants, point to two separate causes for $V_o$ autoinhibition: (i) the interaction of

$a_{NT}$'s distal end with subunit $d$ (Fig. 4, C and D, and fig. S10) and (ii) the uneven spacing of the essential $c$-ring glutamates caused by the position of $c''$E108 (Fig. 1B and fig. S11). This redundancy likely results from evolution to prevent the loss of any existing proton gradient through free $V_o$ generated in response to V-ATPase regulation by reversible disassembly or through incompletely assembled or damaged $V_o$ complexes that lack (or lost) subunit $d$.

## Concluding remarks and outlook

Here, we present the 2.7-Å cryo-EM structure of yeast $V_o$ in lipid nanodisc, revealing previously unseen details of specific protein-lipid interactions, membrane scaffolding proteins, and bound water molecules in the proton path. From all-atom MD simulations, we conclude that proton transfer from $c$-ring essential glutamates is facilitated by alternating access of bulk water that is gated by the protonation state of the proton accepting residue ($a$E789 in this case) at the opening of the luminal half-channel. A second cryo-EM structure, together with MD simulation of $c$-ring rotation, confirms that this rotary dynamics is energetically favorable in the direction of active proton transport. The data also suggest that there are at least two origins for $V_o$ autoinhibition: the interaction of $a_{NT}$ with $d$ and the asymmetry in the spacing of the essential $c$-ring glutamic acid residues. While autoinhibition, $c$-ring asymmetry, and the $a_{NT}$:$d$ interaction are unique to V-ATPase, alternating access of water molecules into the $a$:$c$-ring interface is likely an aspect of rotary ATPase mechanism that is conserved in the related F- and A-ATP synthases. Our studies demonstrate the power of integrating cryo-EM and MD simulations not only to cross-validate the structural models and functional implications but also to be able to explore the dynamic mechanism of this membrane integral nanomotor with atomic detail.

## MATERIALS AND METHODS
### Cryo-EM structure determination
#### Purification and lipid nanodisc reconstitution of yeast $V_o$
The $V_o$ proton channel subcomplex of the yeast $H^+$-V-ATPase was purified and reconstituted into lipid nanodiscs using MSP MSP1E3D1 as described (13, 35).

#### Cryo-EM grid preparation and data acquisition
Three-microliter aliquots of $V_o$ND peak fractions from the Superose size exclusion chromatography run (0.3 mg/ml) were applied to glow-discharged gold grids (UltrAuFoil 1.2/1.3), blotted for 2 to 3 s, and then plunge-frozen in liquid ethane using a Leica EM GP (Leica). The grids were loaded into a Thermo Fisher Titan Krios (300 keV) equipped with a BioQuantum energy filter and a Gatan K2 Summit camera. Movies were acquired in super-resolution electron counting mode with a physical pixel size of 1.08 Å (0.54 Å/pixel in super-resolution mode), an exposure rate of 5 electrons/pixel per second, and a total exposure time of 10 s divided into 25 frames. In-fly frame alignment and dose weighting were performed with MotionCor2 (36), and contrast transfer function (CTF) parameters were estimated with Gctf (37). A total of 4083 movies were then selected based on defocus ranges and CTF quality parameters.

#### Image processing
Each super-resolution movie stack was saved as a new aligned movie stack with 1.08 Å/pixel by MotionCor2 (36) and then imported into RELION3 (38) and CTF corrected using Gctf (37) for further processing (fig. S2, A and B). Aligned micrographs were then generated using RELION3's own implementation for motion correction. The averages of ~200 manually picked particles were used as templates for autopicking. A total of ~1.8 M particles were automatically selected and then, after 2D/3D classification, low-convergence classes were discarded. The remaining ~0.7 M particles were subjected to 3D autorefinement, and the map was subsequently improved by particle-based motion correction, B-factor weighting, and CTF refinement in RELION3 (particle polishing and CTF refinement) (39). At this stage, the resulting map had a resolution of ~3.1 Å as determined according to the gold-standard Fourier shell correlation (FSC) at 0.143 correlation (40). To distinguish potential high-correlating structural heterogeneity, we performed another round of 3D classification ($K = 8$) with a high weighting factor ($T = 20$) and skipping the orientation search (41). Five of eight classes were selected based on visibility of side-chain densities and connectivity. Particles in each class were then subjected to 3D autorefinement to yield final maps with resolutions ranging from 2.7 to 3.6 Å (fig. S2, B and C), with rotational heterogeneity of the $c$-ring representing the main distinguishing feature between classes (fig. S2, D and E). Each final map was processed using nonisotropic B-factor sharpening as implemented in Phenix (42).

#### Focused classification on MSPs of the lipid nanodisc
The density representing the lipid nanodisc was segmented out by removing the protein-derived density using the UCSF (University of California, San Francisco) Chimera (43) and low-pass filtered to generate a mask for the nanodisc. Using the mask, the ~700,000 particles that yielded the 3.1-Å map were subjected to 3D classification without orientation search. The 3D classification revealed substantial heterogeneity of MSP binding to the $V_o$ complex with the predominant population of MSP bound to $V_o$ displayed in Fig. 2 (see also fig. S3).

#### Modeling
Model building was started from our earlier 3.5-Å model [6c6l.pdb; (13)]. The model was iteratively improved using reciprocal and real-space refinement as implemented in Phenix (42), as well as manual model building in Coot (44). For reciprocal space refinement, the box size of the final masked map was reduced to 140 × 124 × 128 pixels and sampled with a d_min of 2.8 Å to generate structure factors. Reciprocal-space refinement included $xyz$ coordinates and individual atom displacement parameters using map phases and Ramachandran restraints. Hydrogens were added to improve geometry and reduce clashes. Each round of reciprocal space refinement was followed by manual model building in Coot and two macro cycles of real-space refinement using global minimization and grid search–based rotamer fitting (grid search–based rotamer fitting was omitted in final stages of the refinement). Model refinement was iterated until quality measures [$R/R_{free}$ in reciprocal-space refinement, MolProbity (45), and EMRinger (46) scores] remained stable. During the refinement process, the pixel size of the map was adjusted from 1.08 to 1.076 Å using the EMRinger score as a measure of quality of fit. Water molecules were placed into distinct density peaks as identified with the "Find Water" routine in Coot using the masked map. The search parameters were 3 root mean square deviation for density peaks and between 2.4 and 3.4 Å for distances to polar side chain or backbone atoms or other water molecules. The automatically placed waters were manually edited to remove waters placed into density belonging to, e.g., lipid molecules or MSP, and to add waters missed due to uncertainties in amino acid side-chain positions. Atomic displacement parameters (B-factors) were estimated using Phenix reciprocal and/or real-space refinement. Lipid molecules and the dolichol-$PP_i$-$GlcNAc_2Man_3$ ligand were modeled using a map that was obtained by masking out density belonging to protein.

Graphical representations of maps and models were generated in the UCSF Chimera (*43*) and visual MD (*47*).

### Structure validation

Proper protein geometry was validated using the validation tools implemented in Coot (*44*), Phenix (*42*), and the MolProbity webserver (*48*). Model-to-map FSC was estimated using phenix.validation_cryoem. The density resolvability for protein and water molecules was evaluated quantitatively as $Q$-score (*21*).

### PISA analysis

Contact areas and binding energies of the interfaces between $c$-ring and $a$ subunit ($a_{CT}$ for $V_o$) were analyzed using the protein interfaces, surfaces and assemblies (PISA) web server (www.ebi.ac.uk/pdbe/pisa/) (*49*).

## MD simulation protocol

### System setup

All MD simulations were initiated using the 2.7-Å model from class 1 (state 3) using NAMD2.12 (*50*). Two computational assays were generated to represent the pre– and post–proton transfer states, whereby $c_{(1)}$E137 was either protonated or deprotonated. Using the membrane builder of the online server CHARMM-GUI (*51*), the protein was embedded in a model membrane with a lipid composition of phosphatidylcholine (PC):phosphatidylethanolamine (PE):phosphatidylinositol (PI):phosphatidylserine (PS) 48%:21%:27%:4% to closely mimic the experimental conditions. The molecular assembly was solvated by 60,196 transferable intermolecular potential with 3 points (TIP3P) water molecules, representing a unit cell of initial dimensions equal to 160 Å by 160 Å by 116 Å. Na$^+$ and Cl$^-$ ions were then added to ensure electric neutrality and set the ionic concentration to 100 mM. The complete computational assay, including the protein, lipids, water molecules, and ions, amounted to nearly 310,000 atoms. After 5000 steps of conjugate-gradient energy minimization, it was simulated for 5 ns at 310 K, with all protein heavy atoms restrained to their initial positions, using a force constant of 5 kcal/mol per Å$^2$. Last, all geometric restraints were removed, and the computational assay was thermalized for 500 ns. Three repeats of the 500-ns MD simulations were performed each for the pre– and post–proton transfer state.

### Simulation protocol

All MD simulations were performed in the isobaric-isothermal ensemble with the MD program NAMD 2.12 and the CHARMM36 all-atom force fields for proteins and lipids. Periodic boundary conditions were applied. The temperature was maintained at 310 K using Langevin dynamics with a damping constant of 0.5 ps$^{-1}$. The pressure was fixed at 1 atm using the Langevin piston method. Van der Waals and electrostatic short-range interactions were smoothly truncated with a 12-Å cutoff, and a switching function was applied at 10 Å. Long-range electrostatic forces were computed with the particle mesh Ewald algorithm. The equations of motion were integrated with the reversible reference system propagation algorithm (r-RESPA) multiple time step propagator, with an effective time step of 2, 2 and 4 fs for bonded, short- and long-range nonbonded contributions, respectively.

### Path-finding simulations

Following the 500-ns equilibration of the computational assay, a constant-velocity simulation was performed, wherein the $c$-ring was rotated by ~14°. The constant-velocity simulation was carried out over a period of 100 ns, with an angular velocity of $10^{-5}$ degree/fs imparted to the $C_\alpha$ atoms of the axial acidic residues of the ring, namely GLU137, GLU108, GLU145, and GLU188. This initial pathway was further refined using the string method with swarm of trajectories in Cartesian space (*27*). Toward this end, 50 equally spaced structures were chosen to form the putative minimum-action pathway, which was evolved in 15 iterations using the average dynamic drift of atomic positions. This dynamic drift was estimated from swarms of 10 trajectories consisting of 10 ps of unbiased MD prefaced by 100 ps of restrained MD at the different nodes of the rotation pathway. The overall string optimization leading to the minimum free energy pathway underlying the 14° rotation of the $c$-ring corresponds to an aggregate simulation of 0.825 μs.

### Free energy calculation

To determine the free energy change associated with the complex conformational transition between conformational states S1 and S2 along the minimum free energy pathway, a path collective variable (PCV) (*52*) was used in conjunction with the multiple-walker extended adaptive biasing force (MW-eABF) algorithm (*29*, *53*). A PCV allows progress along the minimum free energy pathway to be described by means of a differentiable mathematical expression

$$s(\mathbf{x}) = \frac{1}{N-1} \frac{\sum_i (i-1)\, e^{-\lambda(\mathbf{x}-\mathbf{x}_i)^2}}{\sum_i e^{-\lambda(\mathbf{x}-\mathbf{x}_i)^2}}$$

wherein $i$ varies between 1 and $N$, the number of intermediate structures forming the discretized minimum free energy pathway. The mean square displacements, $(\mathbf{x} - \mathbf{x}_i)^2$, were determined based on the positions of the $C_\alpha$ and $C_\beta$ atoms of the $c$-ring in its instantaneous conformation, $\mathbf{x}$, and that of the $i$th intermediate state, $\mathbf{x}_i$, of the minimum free energy pathway. $\lambda$ is a smoothing factor comparable to the inverse of mean square displacement between successive intermediates. An ancillary variable was used to measure deviations from the minimum free energy pathway and confine sampling in a tube wrapping around the latter

$$z(\mathbf{x}) = -\frac{1}{\lambda} \ln\left( \sum_i e^{-\lambda(\mathbf{x}-\mathbf{x}_i)^2} \right)$$

Loose geometric restraints were applied to ensure that the trajectory samples conformational space within a tube centered on the minimum free energy pathway and of radius equal to 2.5 Å. The 50 intermediate structures served as the initial conformations of the 50 walkers in the MW-eABF simulation. The gradients of the free energy landscape measured by each walker were exchanged every 10 ps. The primary PCV, $s(\mathbf{x})$, was discretized in bins 0.1 Å wide, wherein samples of the local force were accrued. The time-dependent bias was applied once a threshold of 5000 samples was attained. Each walker was sampled for 100 ns, so a cumulative simulation of 100 ns/walker × 50 walker = 5 μs was performed for wild type and $c''$E108A $V_o$ $c$-ring. The statistics derived from these simulations are reweighted into a convergent free energy or the so-called "potential of mean force" profile, presented in Fig. 4 and fig. S12.

### Kinetics calculation

Kinetics calculations provide an estimate of the mean first passage time, τ, which is the inverse of the rate constant $k$. Assuming a diffusion-dominated motion of the protein in the membrane environment, and a position-independent diffusivity over the entire reaction pathway, equal to $D = 6 \times 10^8$ Å$^2$/s (*54*–*56*), the free energy profile obtained from the eABF simulations can be reconciled with the mean first passage time using the following expression (*57*)

$$\tau = \frac{1}{k} = \sum_{i=0}^{N} \frac{\sum_{j=0}^{i} e^{-\beta w(s_j)}}{D\, e^{-\beta w(s_i)}}$$

where the transition pathway is discretized over the $N$ points of the curvilinear pathway, and $w(s)$ is the accompanying free energy change. The quantity appearing in the main sum represents the probability of finding the system at point $s_i$ along the transition pathway.

## SUPPLEMENTARY MATERIALS

Supplementary material for this article is available at http://advances.sciencemag.org/cgi/content/full/6/41/eabb9605/DC1

## REFERENCES AND NOTES

1. K. Cotter, L. Stransky, C. McGuire, M. Forgac, Recent insights into the structure, regulation, and function of the V-ATPases. *Trends Biochem. Sci.* **40**, 611–622 (2015).
2. V. Marshansky, M. Futai, The V-type $H^+$-ATPase in vesicular trafficking: Targeting, regulation and function. *Curr. Opin. Cell Biol.* **20**, 415–426 (2008).
3. P. M. Kane, The where, when, and how of organelle acidification by the yeast vacuolar $H^+$-ATPase. *Microbiol. Mol. Biol. Rev.* **70**, 177–191 (2006).
4. M. A. Harrison, S. P. Muench, The vacuolar ATPase—A nano-scale motor that drives cell biology. *Subcell. Biochem.* **87**, 409–459 (2018).
5. P. M. Kane, Disassembly and reassembly of the yeast vacuolar $H^+$-ATPase in vivo. *J. Biol. Chem.* **270**, 17025–17032 (1995).
6. R. A. Oot, S. Couoh-Cardel, S. Sharma, N. J. Stam, S. Wilkens, Breaking up and making up: The secret life of the vacuolar $H^+$-ATPase. *Protein Sci.* **26**, 896–909 (2017).
7. A. Hahn, J. Vonck, D. J. Mills, T. Meier, W. Kühlbrandt, Structure, mechanism, and regulation of the chloroplast ATP synthase. *Science* **360**, eaat4318 (2018).
8. H. Guo, T. Suzuki, J. L. Rubinstein, Structure of a bacterial ATP synthase. *eLife* **8**, e43128 (2019).
9. B. J. Murphy, N. Klusch, J. Langer, D. J. Mills, Ö. Yildiz, W. Kühlbrandt, Rotary substates of mitochondrial ATP synthase reveal the basis of flexible $F_1$-$F_o$ coupling. *Science* **364**, eaaw9128 (2019).
10. L. Zhou, L. A. Sazanov, Structure and conformational plasticity of the intact *Thermus thermophilus* V/A-type ATPase. *Science* **365**, eaaw9144 (2019).
11. O. Jardetzky, Simple allosteric model for membrane pumps. *Nature* **211**, 969–970 (1966).
12. M. T. Mazhab-Jafari, A. Rohou, C. Schmidt, S. A. Bueler, S. Benlekbir, C. V. Robinson, J. L. Rubinstein, Atomic model for the membrane-embedded $V_O$ motor of a eukaryotic V-ATPase. *Nature* **539**, 118–122 (2016).
13. S.-H. Roh, N. J. Stam, C. F. Hryc, S. Couoh-Cardel, G. Pintilie, W. Chiu, S. Wilkens, The 3.5-Å CryoEM structure of nanodisc-reconstituted yeast vacuolar ATPase $V_O$ proton channel. *Mol. Cell* **69**, 993–1004.e3 (2018).
14. T. Vasanthakumar, S. A. Bueler, D. Wu, V. Beilsten-Edmands, C. V. Robinson, J. L. Rubinstein, Structural comparison of the vacuolar and Golgi V-ATPases from *Saccharomyces cerevisiae*. *Proc. Natl. Acad. Sci. U.S.A.* **116**, 7272–7277 (2019).
15. D. Pogoryelov, Ö. Yildiz, J. D. Faraldo-Gómez, T. Meier, High-resolution structure of the rotor ring of a proton-dependent ATP synthase. *Nat. Struct. Mol. Biol.* **16**, 1068–1073 (2009).
16. M. Toei, S. Toei, M. Forgac, Definition of membrane topology and identification of residues important for transport in subunit a of the vacuolar ATPase. *J. Biol. Chem.* **286**, 35176–35186 (2011).
17. Y. Gao, E. Cao, D. Julius, Y. Cheng, TRPV1 structures in nanodiscs reveal mechanisms of ligand and lipid action. *Nature* **534**, 347–351 (2016).
18. D. W. Borhani, D. P. Rogers, J. A. Engler, C. G. Brouillette, Crystal structure of truncated human apolipoprotein A-I suggests a lipid-bound conformation. *Proc. Natl. Acad. Sci. U.S.A.* **94**, 12291–12296 (1997).
19. Z. Fang, C. B. Marshall, T. Nishikawa, A. D. Gossert, J. M. Jansen, W. Jahnke, M. Ikura, Inhibition of K-RAS4B by a unique mechanism of action: Stabilizing membrane-dependent occlusion of the effector-binding site. *Cell Chem. Biol.* **25**, 1327–1336.e4 (2018).
20. S. Dang, M. K. van Goor, D. Asarnow, Y. Wang, D. Julius, Y. Cheng, J. van der Wijst, Structural insight into TRPV5 channel function and modulation. *Proc. Natl. Acad. Sci. U.S.A.* **116**, 8869–8878 (2019).
21. G. Pintilie, K. Zhang, Z. Su, S. Li, M. F. Schmid, W. Chiu, Measurement of atom resolvability in cryo-EM maps with $Q$-scores. *Nat. Methods* **17**, 328–334 (2020).
22. M. Nakasako, Water-protein interactions from high-resolution protein crystallography. *Philos. Trans. R. Soc. Lond. B Biol. Sci.* **359**, 1191–1206 (2004).
23. B. C. Goh, J. A. Hadden, R. C. Bernardi, A. Singharoy, R. McGreevy, T. Rudack, C. K. Cassidy, K. Schulten, Computational methodologies for real-space structural refinement of large macromolecular complexes. *Annu. Rev. Biophys.* **45**, 253–278 (2016).
24. R. S. Negrin, D. L. Foster, R. H. Fillingame, Energy-transducing $H^+$-ATPase of *Escherichia coli*. Reconstitution of proton translocation activity of the intrinsic membrane sector. *J. Biol. Chem.* **255**, 5643–5648 (1980).
25. J. Zhang, M. Myers, M. Forgac, Characterization of the $V_0$ domain of the coated vesicle ($H^+$)-ATPase. *J. Biol. Chem.* **267**, 9773–9778 (1992).
26. E. Uchida, Y. Ohsumi, Y. Anraku, Purification and properties of $H^+$-translocating, $Mg^{2+}$-adenosine triphosphatase from vacuolar membranes of *Saccharomyces cerevisiae*. *J. Biol. Chem.* **260**, 1090–1095 (1985).
27. A. C. Pan, D. Sezer, B. Roux, Finding transition pathways using the string method with swarms of trajectories. *J. Phys. Chem. B* **112**, 3432–3440 (2008).
28. A. Singharoy, C. Chipot, M. Moradi, K. Schulten, Chemomechanical coupling in hexameric protein-protein interfaces harnesses energy within V-Type ATPases. *J. Am. Chem. Soc.* **139**, 293–310 (2017).
29. H. Fu, X. Shao, C. Cai, C. Chipot, Taming rugged free energy landscapes using an average force. *Acc. Chem. Res.* **52**, 3254–3264 (2019).
30. S. Wilkens, Z. Zhang, Y. Zheng, A structural model of the vacuolar ATPase from transmission electron microscopy. *Micron* **36**, 109–126 (2005).
31. J. Qi, M. Forgac, Function and subunit interactions of the N-terminal domain of subunit a (Vph1p) of the yeast V-ATPase. *J. Biol. Chem.* **283**, 19274–19282 (2008).
32. S. Couoh-Cardel, E. Milgrom, S. Wilkens, Affinity purification and structural features of the yeast vacuolar ATPase $V_o$ membrane sector. *J. Biol. Chem.* **290**, 27959–27971 (2015).
33. C. Etzold, G. Deckers-Hebestreit, K. Altendorf, Turnover number of *Escherichia coli* $F_0F_1$ ATP synthase for ATP synthesis in membrane vesicles. *Eur. J. Biochem.* **243**, 336–343 (1997).
34. R. Hirata, L. A. Graham, A. Takatsuki, T. H. Stevens, Y. Anraku, VMA11 and VMA16 encode second and third proteolipid subunits of the *Saccharomyces cerevisiae* vacuolar membrane $H^+$-ATPase. *J. Biol. Chem.* **272**, 4795–4803 (1997).
35. N. J. Stam, S. Wilkens, Structure of the lipid nanodisc-reconstituted vacuolar ATPase proton channel: Definition of the interaction of rotor and stator and implications for enzyme regulation by reversible dissociation. *J. Biol. Chem.* **292**, 1749–1761 (2017).
36. S. Q. Zheng, E. Palovcak, J.-P. Armache, K. A. Verba, Y. Cheng, D. A. Agard, MotionCor2: Anisotropic correction of beam-induced motion for improved cryo-electron microscopy. *Nat. Methods* **14**, 331–332 (2017).
37. K. Zhang, Gctf: Real-time CTF determination and correction. *J. Struct. Biol.* **193**, 1–12 (2016).
38. J. Zivanov, T. Nakane, B. O. Forsberg, D. Kimanius, W. J. H. Hagen, E. Lindahl, S. H. W. Scheres, New tools for automated high-resolution cryo-EM structure determination in RELION-3. *eLife* **7**, e42166 (2018).
39. J. Zivanov, T. Nakane, S. H. W. Scheres, A Bayesian approach to beam-induced motion correction in cryo-EM single-particle analysis. *IUCrJ* **6**, 5–17 (2019).
40. S. Chen, G. McMullan, A. R. Faruqi, G. N. Murshudov, J. M. Short, S. H. W. Scheres, R. Henderson, High-resolution noise substitution to measure overfitting and validate resolution in 3D structure determination by single particle electron cryomicroscopy. *Ultramicroscopy* **135**, 24–35 (2013).
41. X.-c. Bai, E. Rajendra, G. Yang, Y. Shi, S. H. W. Scheres, Sampling the conformational space of the catalytic subunit of human γ-secretase. *eLife* **4**, e11182 (2015).
42. P. D. Adams, P. V. Afonine, G. Bunkóczi, V. B. Chen, I. W. Davis, N. Echols, J. J. Headd, L.-W. Hung, G. J. Kapral, R. W. Grosse-Kunstleve, A. J. McCoy, N. W. Moriarty, R. Oeffner, R. J. Read, D. C. Richardson, J. S. Richardson, T. C. Terwilliger, P. H. Zwart, PHENIX: A comprehensive Python-based system for macromolecular structure solution. *Acta Crystallogr. D Biol. Crystallogr.* **66**, 213–221 (2010).
43. E. F. Pettersen, T. D. Goddard, C. C. Huang, G. S. Couch, D. M. Greenblatt, E. C. Meng, T. E. Ferrin, UCSF Chimera—A visualization system for exploratory research and analysis. *J. Comput. Chem.* **25**, 1605–1612 (2004).
44. P. Emsley, B. Lohkamp, W. G. Scott, K. Cowtan, Features and development of Coot. *Acta Crystallogr. D Biol. Crystallogr.* **66**, 486–501 (2010).
45. V. B. Chen, W. B. Arendall III, J. J. Headd, D. A. Keedy, R. M. Immormino, G. J. Kapral, L. W. Murray, J. S. Richardson, D. C. Richardson, MolProbity: All-atom structure validation for macromolecular crystallography. *Acta Crystallogr. D Biol. Crystallogr.* **66**, 12–21 (2010).
46. B. A. Barad, N. Echols, R. Y.-R. Wang, Y. Cheng, F. DiMaio, P. D. Adams, J. S. Fraser, EMRinger: Side chain-directed model and map validation for 3D cryo-electron microscopy. *Nat. Methods* **12**, 943–946 (2015).
47. W. Humphrey, A. Dalke, K. Schulten, VMD: Visual molecular dynamics. *J. Mol. Graph.* **14**, 33–38 (1996).
48. C. J. Williams, J. J. Headd, N. W. Moriarty, M. G. Prisant, L. L. Videau, L. N. Deis, V. Verma, D. A. Keedy, B. J. Hintze, V. B. Chen, S. Jain, S. M. Lewis, W. B. Arendall III, J. Snoeyink, P. D. Adams, S. C. Lovell, J. S. Richardson, D. C. Richardson, MolProbity: More and better reference data for improved all-atom structure validation. *Protein Sci.* **27**, 293–315 (2018).
49. E. Krissinel, K. Henrick, Inference of macromolecular assemblies from crystalline state. *J. Mol. Biol.* **372**, 774–797 (2007).
50. J. C. Phillips, R. Braun, W. Wang, J. Gumbart, E. Tajkhorshid, E. Villa, C. Chipot, R. D. Skeel, L. Kalé, K. Schulten, Scalable molecular dynamics with NAMD. *J. Comput. Chem.* **26**, 1781–1802 (2005).

51. S. Jo, T. Kim, V. G. Iyer, W. Im, CHARMM-GUI: A web-based graphical user interface for CHARMM. *J. Comput. Chem.* **29**, 1859–1865 (2008).

52. F. Pietrucci, Strategies for the exploration of free energy landscapes: Unity in diversity and challenges ahead. *Rev. Phys.* **2**, 32–45 (2017).

53. J. Comer, J. C. Phillips, K. Schulten, C. Chipot, Multiple-replica strategies for free-energy calculations in NAMD: Multiple-walker adaptive biasing force and walker selection rules. *J. Chem. Theory Comput.* **10**, 5276–5285 (2014).

54. A. Aksimentiev, I. A. Balabin, R. H. Fillingame, K. Schulten, Insights into the molecular mechanism of rotation in the $F_o$ sector of ATP synthase. *Biophys. J.* **86**, 1332–1344 (2004).

55. T. Elston, H. Wang, G. Oster, Energy transduction in ATP synthase. *Nature* **391**, 510–513 (1998).

56. K. Weiß, A. Neef, Q. Van, S. Kramer, I. Gregor, J. Enderlein, Quantifying the diffusion of membrane proteins and peptides in black lipid membranes with 2-focus fluorescence correlation spectroscopy. *Biophys. J.* **105**, 455–462 (2013).

57. A. Szabo, K. Schulten, Z. Schulten, First passage time approach to diffusion controlled reactions. *J. Chem. Phys.* **72**, 4350 (1980).

58. S. Esmail, N. Kartner, Y. Yao, J. W. Kim, R. A. F. Reithmeier, M. F. Manolson, N-linked glycosylation of a subunit isoforms is critical for vertebrate vacuolar $H^+$-ATPase (V-ATPase) biosynthesis. *J. Cell. Biochem.* **119**, 861–875 (2018).

59. A. P. Srivastava, M. Luo, W. Zhou, J. Symersky, D. Bai, M. G. Chambers, J. D. Faraldo-Gómez, M. Liao, D. M. Mueller, High-resolution cryo-EM analysis of the yeast ATP synthase in a lipid membrane. *Science* **360**, eaas9699 (2018).

60. C. Bai, A. Warshel, Revisiting the protomotive vectorial motion of $F_0$-ATPase. *Proc. Natl. Acad. Sci. U.S.A.* **116**, 19484–19489 (2019).

61. T. Hirata, N. Nakamura, H. Omote, Y. Wada, M. Futai, Regulation and reversibility of vacuolar $H^+$-ATPase. *J. Biol. Chem.* **275**, 386–389 (2000).

**Citation:** S.-H. Roh, M. Shekhar, G. Pintilie, C. Chipot, S. Wilkens, A. Singharoy, W. Chiu, Cryo-EM and MD infer water-mediated proton transport and autoinhibition mechanisms of $V_o$ complex. *Sci. Adv.* **6**, eabb9605 (2020).

# Science Advances

## Cryo-EM and MD infer water-mediated proton transport and autoinhibition mechanisms of $V_O$ complex

Soung-Hun Roh, Mrinal Shekhar, Grigore Pintilie, Christophe Chipot, Stephan Wilkens, Abhishek Singharoy and Wah Chiu

| | |
|---|---|
| **ARTICLE TOOLS** | http://advances.sciencemag.org/content/6/41/eabb9605 |
| **SUPPLEMENTARY MATERIALS** | http://advances.sciencemag.org/content/suppl/2020/10/05/6.41.eabb9605.DC1 |
| **REFERENCES** | This article cites 61 articles, 19 of which you can access for free<br>http://advances.sciencemag.org/content/6/41/eabb9605#BIBL |
| **PERMISSIONS** | http://www.sciencemag.org/help/reprints-and-permissions |

Use of this article is subject to the Terms of Service